

Direct detection of dark matter at LUX-ZEPLIN

Mariana Letra^{1,a}, Paulo Pires^{1,b}, and Pedro Sá^{1,c}

¹Universidade de Coimbra, Coimbra, Portugal

Project supervisor: C. Silva, P. Brás

October 20, 2022

Abstract. Nowadays, it's consensual that Dark matter constitutes 85% of the mass in the universe. Even though there is plentiful evidence of dark matter, its nature is still unknown, posing a central problem in modern physics. Weakly Interactive Massive Particles (WIMPs) are still a strong candidate for dark matter. One of the lead experiments specialized in searching for these particles is the LUX-ZEPLIN experiment. Our study presents the process of detection and data analysis for a search of WIMP dark matter with LZ. With 15 days of simulated LZ data, a limit on the SI WIMP-nucleon cross-section of $1.856 \cdot 10^{-47} \text{ cm}^2$ was obtained (90% CL).

KEYWORDS: Dark matter, LUX-ZEPLIN, WIMPs

1 Introduction

1.1 Dark Matter

The nature of dark matter is presently a major question for both cosmology and particle physics. However, its existence is still debated and relies on the observations of gravitational effects in large-scale structures and cosmology. Dark matter refers to the distribution of an unknown mass in the universe that does not interact with electromagnetic radiation. There are plentiful evidence of the existence of dark matter. One of the most striking evidence of unexpected gravitational effects comes from galaxies, in particular spiral galaxies. In spiral galaxies, most of the visible mass is gathered in the budge and the disc. The velocity of stars v at a distance R from the galactic centre is given by:

$$v(R) = \sqrt{\frac{GM(R)}{R}} \quad (1)$$

where G is the gravitational constant and $M(R)$ is the total mass contained in a sphere of radius R . Far from the centre, the disc fades away so that the star density decreases and the total mass inside the radius R becomes constant. As a consequence, the velocity is expected to decrease as $v(R) \propto R^{-1/2}$. However, for most of the spiral galaxies, the observed velocity far from the centre is approximately constant, see Fig.1, something that can be explained by the presence of large quantities of mass far beyond the fading of the visible disc. Since most of the matter in the halo is invisible, its mass is considered to mainly come from dark matter.

Further evidence for dark matter comes from measurements on cosmological scales of anisotropies in the cosmic microwave background. In the primordial universe, electrons combined with protons to form hydrogen atoms, this led to a lower free-electron density which allowed the photons to move freely for the first time. Those photons registered the local thermal energy just before decoupling from baryonic matter, being called the cosmic microwave

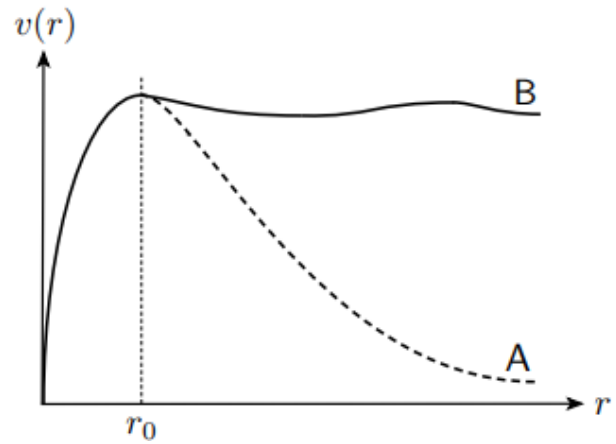


Figure 1. A typical galaxy rotation curve, A and B represent the predicted and observed velocity respectively [1].

background. This radiation has oscillations and its value depends on the region of the sky they are being detected. These oscillations are related to the local density of matter and energy. The angular scale and height of the peaks of these oscillations are powerful probes of cosmological parameters, including the total energy density, the baryonic fraction, and the dark matter components, as shown in Fig.2. The height of the second peak implies that 5% of the total energy is ordinary atoms, while matching all the peaks implies that 26% of the total is dark matter [2]. Indeed the cosmic background radiation by itself provides irrefutable evidence for dark matter.

1.2 Direct Detection

The main experimental methods to detect dark matter are direct detection, indirect detection and production. Direct detection consists of the detection of dark matter particles on Earth. This method should be reliable since the local density of dark matter in the Solar System is approximately 0.4 GeV/cm^3 [3]. If dark matter is composed, for example, of particles with masses around 100 GeV, this results in about 4 particles per cubic meter, so, during one

^ae-mail: marianaletra361@gmail.com

^be-mail: paulopires2002@gmail.com

^ce-mail: pbtcs2@gmail.com

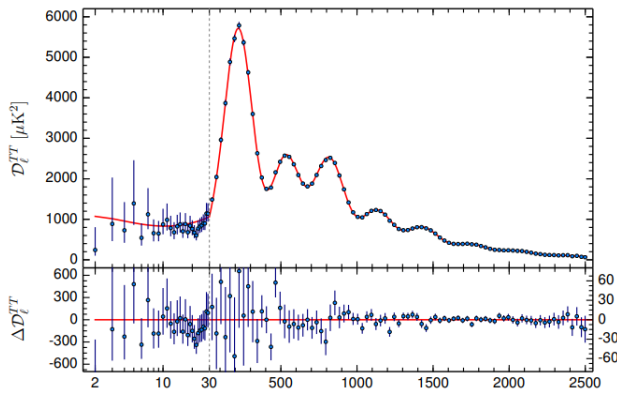


Figure 2. Planck's power spectrum of temperature fluctuations in the cosmic microwave background. The blue dots with error bars are the Planck data, and the red curve represents the best fit to the data according to the standard model of cosmology [2].

year each cubic meter on Earth would be crossed by $\sim 10^{13}$ dark matter particles. It is thus possible to look for interactions of dark matter particles on Earth by building large tanks and detectors of specific materials which maximize the probability of interaction. The idea is to measure the energy deposited by a WIMP scattering with a nucleus of the target material to detect their interactions with matter and to estimate the dark matter mass and the scattering cross-section with nucleons, σ_N .

1.3 WIMPs

The observations reveal that particle dark matter must be massive, stable over billions of years, very likely collisionless, interacting mostly gravitationally and distinct from baryonic matter. The evidence from cosmic background radiation and the form of cosmic structures indicates that dark matter is non-relativistic, and thus dubbed as "cold". The Weakly Interactive Massive Particles (WIMPs) are one of the strongest candidates for cold dark matter [4]. WIMPs are theorized to be massive particles with a range of mass between 1 and 10^5 GeV and chargeless. It is assumed that they were thermally produced in the Early Universe. It is expected that these particles could produce detectable signals from recoiling nuclei if they interact with baryonic matter in any way other than gravitationally.

2 LUX-ZEPLIN Experiment

LUX-ZEPLIN (LZ) is a next-generation dark matter experiment located at the Sanford Underground Research Facility in Lead, South Dakota, US [5]. The main purpose of the experiment is to detect WIMPs directly, but the extremely low background environment allows the study of other rare events. On July 7, 2022, LZ presented their first science results and reached a world-leading sensitivity to WIMP-nucleon SI interaction Fig.3 [6].

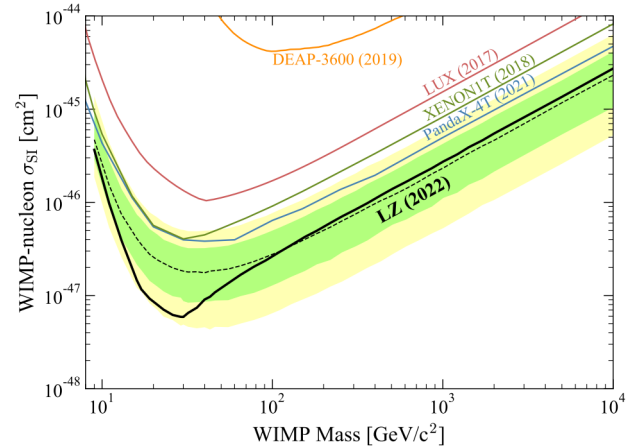


Figure 3. Limit on the spin-independent (SI) WIMP-nucleon cross-section from the first science run of LZ. The black line represents the 90% confidence limit for the spin-independent WIMP cross-section vs. WIMP mass. The green and yellow bands are the 1 and 2 sensitivity bands. The dotted line shows the median of the sensitivity projection. Also shown are some other experiments limits[6].

2.1 Detector Description

The LZ experiment uses 7 tonnes of active liquid xenon to search for nuclear recoils from WIMPs. The active liquid xenon is inside a double walled titanium cryostat with 1.5 m of both diameter and height, with an applied electric field to form a Time Projection Chamber (TPC) Sec. 2.2. The drift and extraction fields in the TPC are generated by grid electrodes made of woven stainless steel. The drift field is generated between the cathode grid at the bottom of the TPC and the gate grid just below the liquid xenon surface, while the much stronger extraction field is generated between the gate grid and the anode grid that is just above the liquid surface [7]. The relatively large density of liquid xenon allows the TPC to "self-shield" from external radiation, meaning that the innermost volume, or "fiducial" volume, of the detector is largely background-free. At the top and bottom part of the TPC there are photomultiplier tubes (PMT) that detect Xe scintillation light from the energy depositions inside the detector. The detector is surrounded by a skin of 3 tonnes of liquid xenon equipped with a PMT readout too. Outside the detector there are a series of layers of active and passive shielding to reduce the background, mainly from gamma rays and neutrons, the latter being able to reproduce the signature of a WIMP interaction that would be created by WIMPs. The double-walled vacuum insulated titanium cryostat is surrounded by a Gadolinium outer detector that is monitored with a suite of PTMs. The entire instrument is immersed in a 220-tonne water tank to provide extra passive shielding and muon tagging [8]. Fig.4 represents a graphic description of the entire structure.

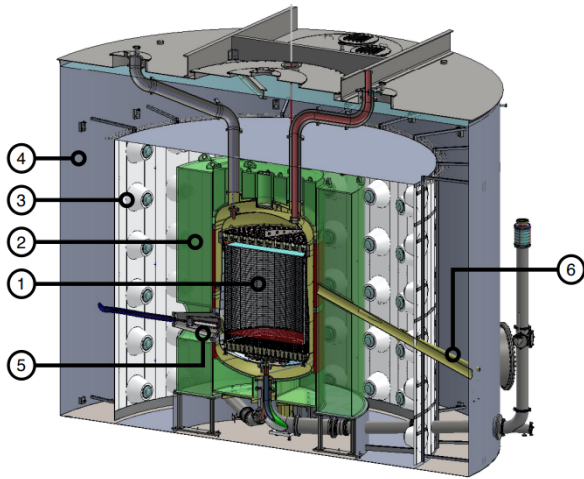


Figure 4. Schematic of the LZ experiment, showing the major detector subsystems. Liquid xenon TPC (1). GdLS outer detector (2). Outer detector PTMs (3). Water shield (4). The cathode high voltage connection (5). Neutron calibration source conduit tank (6) [8].

2.2 Time Projection Chamber

A time projection chamber, like the one in the LZ experiment, is a type of particle detector that uses a combination of electromagnetic fields with a sensitive target volume to perform a three-dimensional reconstruction of a particle trajectory or interaction. The working principle is as follows: when a collision deposits energy inside the active LXe volume of the detector, some prompt scintillation light is generated, along with some ionization and heat. The scintillation light (S1) is promptly detected at the top and bottom PTMs arrays. The ionization electrons drift upwards by the electric field applied and are extracted to the gas xenon layer on the top of the TPC by the strong extraction field, where they emit photo-luminescence light (S2), being then detected mostly at the top array of PTMs [9]. A scheme of the detection process is represented at Fig.5. Both S1 and S2 signals allow us to reconstruct the information about the collision inside the chamber:

Depth: The time difference between the prompt S1 light and the delayed S2 light provides us with the depth of the interaction;

XY position: Since S2 light is created very close to the top PTM array, the XY position where the collision occurred can be reconstructed;

Energy deposited: The S1 and S2 signals are related to the energy deposited and are used to reconstruct the energy Sec. 3.3.

Since S2 light is created at the top layer of the liquid xenon, being then closer to the PTMs, it alone can give us the XY position where the collision occurred.

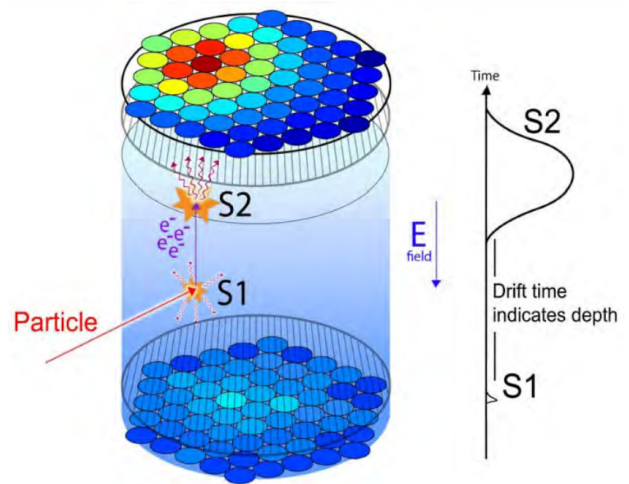


Figure 5. Scheme of the TPC working principle. Each particle interaction in the liquid xenon produces S1 light and S2 light. This allows precise location in three dimensions, energy reconstruction and discrimination between nuclear and electronic recoils [9].

2.3 Nuclear recoils and electronic recoils discrimination

When a collision occurs, it can be either an electron recoil where the incoming particle interacts with the atomic electrons, and nuclear recoil, where the incoming particle interacts with the nucleus. Electron recoils can occur in interactions with beta particles and gamma particles, while nuclear recoils can be caused by alpha particles, neutrons or WIMPs. Therefore, it's important to discriminate between these two types of recoil. For the same deposited energy, nuclear recoils release more energy in the form of heat than electronic recoils, and this translates to a lower S2/S1 signal ratio, see Fig.6. This difference in the ratio S2/S1 allows us to discriminate between each recoil.

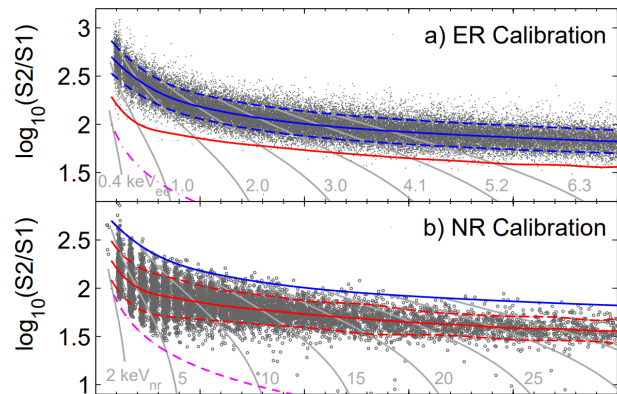


Figure 6. Calibrations of the detector response in the fiducial volume using LUX data. The ER (tritium) calibration (a) and the NR calibration (obtained with mono-energetic neutrons from a D-D generator) (b). The continuous lines show the band means, and the dashed lines indicate the $\pm 1.28\sigma$ contours. The S2 threshold applied is represented in magenta [10].

3 Data analysis

For our analysis, we used simulated data computed with the software package BACCARAT that uses Geant4 and NEST [11]. This data was obtained from ultra-precise simulations of the detector's geometry and of the physics processes of the radiation's interaction with matter.

3.1 Background

Despite all passive and active shielding, a detector as sensible as LZ is still susceptible to some background noise. Besides external radiation sources, these backgrounds can have two causes: radioactive decays of the materials used in the TPC and contamination mixed in the xenon itself. While noise due to the contamination of the xenon is uniform throughout the detector, contamination from detector materials concentrates at the walls and grids of the detector, see Fig.7.

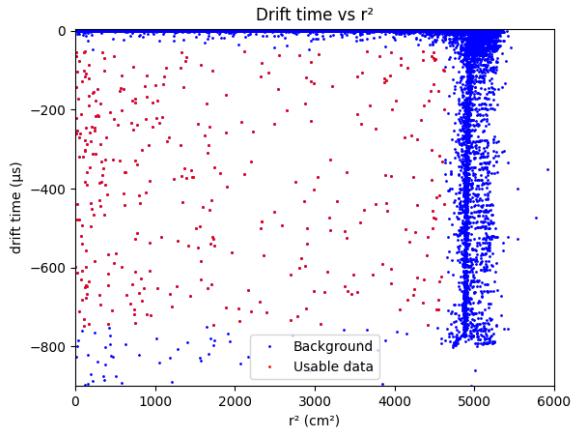


Figure 7. Drift time vs r^2 , for WIMP Search simulated data, with the discrimination between background noise and usable data. The blue dots represent the data removed with the fiducial cut, and the red dots the valid data.

To eliminate this noise a fiducial cut was defined, limiting the values of the radius and drift time to:

$$50 < \text{Drift Time } (\mu\text{s}) < 800$$

$$0 < \text{Radius (cm)} < 68$$

The cut made in the drift time comes from the relation between drift time and depth, see Sec. 2.2, being $50 \mu\text{s}$ correspondent to the depth of the liquid-gaseous xenon interface and $800 \mu\text{s}$ to the bottom of the TPC. The radial cut rejects the backgrounds near the wall and misconstrued events close to the edges of the TPC. This fiducial volume is the same used for the sensitivity analysis of LZ [12].

3.2 Position corrections

Since the characteristics of the TPC influence the detected signals, some corrections over position have to be made

to normalize the data to a specific reference point in the detector. To make these corrections, it was used simulated data of a uniform distribution of Xe-131m in the active volume of the LZ. A clear dependence can be seen in the plot of the S2 signal vs drift time, see Fig.8.

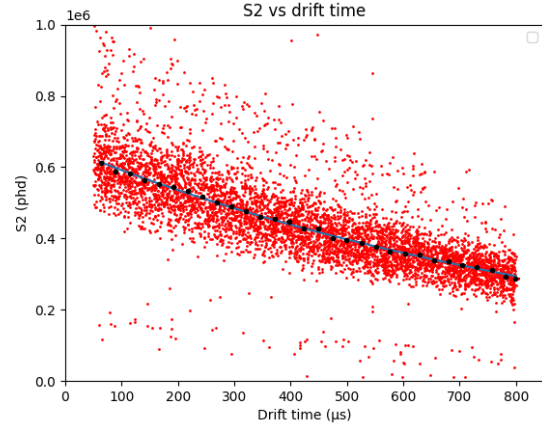


Figure 8. S2 signal dependency with drift time. The black line represents the fit used to adjust the data.

This dependency is due to the probability of electron recombination with electronegative impurities mixed with the xenon, which increases with drift lengths, resulting in charge loss and smaller S2 signals. As an electron has to travel a further distance, the probability of occurring a recombination grows exponentially, preventing the electrons from reaching the extraction region and producing the S2 signal. To correct this dependency, the data is adjusted with equation 2:

$$S2_{unc} = S2_{corr} \cdot e^{-\tau/EL} \quad (2)$$

where τ is the drift time, EL the electron's lifetime inside the TPC, $S2_{unc}$ is the raw S2 signal's data and $S2_{corr}$ is the S2 signal at the top of the TPC ($50 \mu\text{s}$), being this position where the electrons are going to drift a shorter distance. With the parameters obtained from the fit we got an electron's lifetime (EL) of 1 ms. With the parameters from the previous fit, it's possible to correct the S2 signal's dependency on the drift time, see Fig.9.

Through the graphic of the S2 signal vs r^2 a dependency is evident and needs to be corrected as well, see Fig.10.

This dependency can be due to: the PMTs subtended solid angle being larger for events that occur in the center of the TPC and decreasing with proximity to the walls or the fact that the material used in the walls of the gaseous xenon phase (kapton) has a low reflectivity. This material can absorb the electroluminescence light before it reaches the detectors, decreasing the S2 signal near the walls.

This dependency was corrected with an exponential fit, see Fig.10. The parameters obtained were used to correct the data, Fig.11.

The same analysis was made for the S1 signal. This signal also depended on the drift time, see Fig.12.

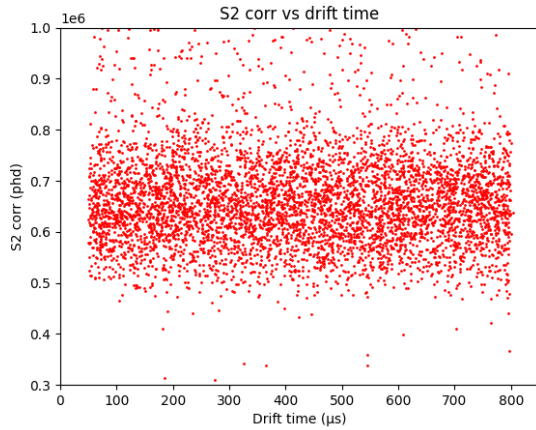


Figure 9. Corrected S2 signal ($S2_{corr}$) signal vs drift time.

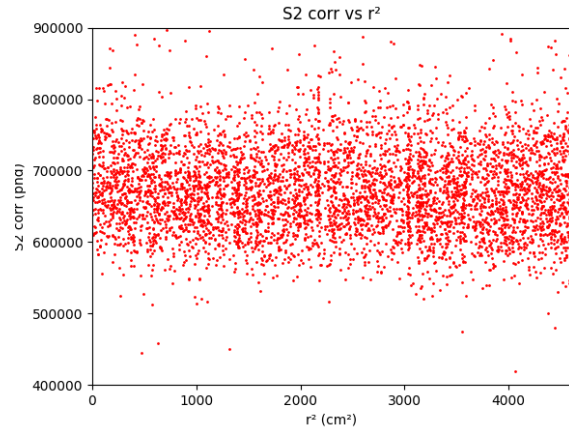


Figure 11. Electroluminescence light signal vs r^2

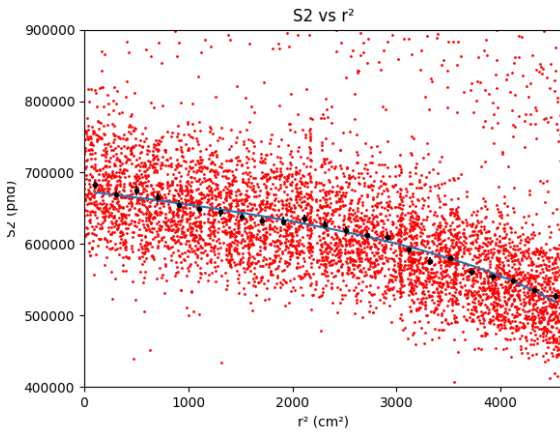


Figure 10. S2 signal vs r^2 , it is represented the S2 signal's dependency with r^2 and the fit used to adjust the data.

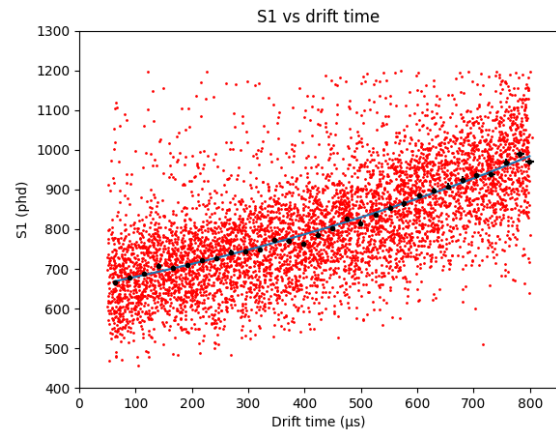


Figure 12. S1 signal's dependency on the drift time and the fit used to adjust the data

This dependency can be due to geometrical effects in the TPC. Once again, it was possible to correct this dependency with exponential or polynomial fits. The fit shown on Fig.12 is an exponential fit. With the parameters obtained, we got the corrected S1 signal.

This dependency was corrected with an exponential fit, see Fig.12. Since the S1 light is equally emitted from the center of the TPC to both arrays of PTMs (top and bottom), the correction of the signal was normalized for a drift time of $450 \mu s$, corresponding to the geometrical center of the sensitive zone of the TPC. The parameters obtained were used to correct the data, Fig.13.

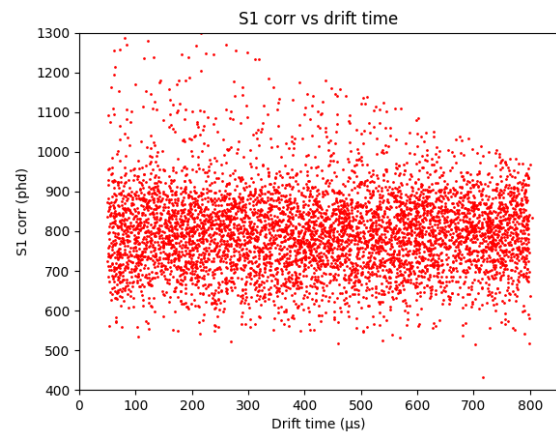


Figure 13. $S1_{corr}$ signal vs drift time, the dependency was indeed corrected.

In the fiducial volume, the S1 signal's dependency with r^2 is very small, so it was ignored in the preliminary analysis.

3.3 Energy Reconstruction

With all the previous corrections it is possible to reconstruct the deposited energy of a particle, using simulated data of Xe-131m and Kr-83m. The energy reconstruction is given by the equation 4 [13]:

$$E = \frac{W_q}{L(E)} \left[\frac{S1}{g_1} + \frac{S2}{g_2} \right] \quad (3)$$

where $W_q = 13.7$ eV is the average energy to produce a single quanta, $L(E)$ is the Lindhart's factor, being $L(E) = 1$ for electronic recoils and $L(E) \approx 0.2$ for nuclear recoils, g_1 is the fraction of detected photons by emitted scintillation photons and g_2 is the number of photons detected by electrons extracted from the recoil track. It is possible to obtain both efficiency factors, g_1 and g_2 , with two known energy gamma decays, such as Xe-131m with energy of 164 keV [14] and Kr-83m with energy of 41.5 keV [15]. From sets of simulated events of Xe-131m and Kr-83m, the efficiency factors were determined using the equation 4, by plotting, for both sets, $\langle S2 \rangle / E$ in function of $\langle S1 \rangle / E$ and fitting a linear regression, see Fig.14.

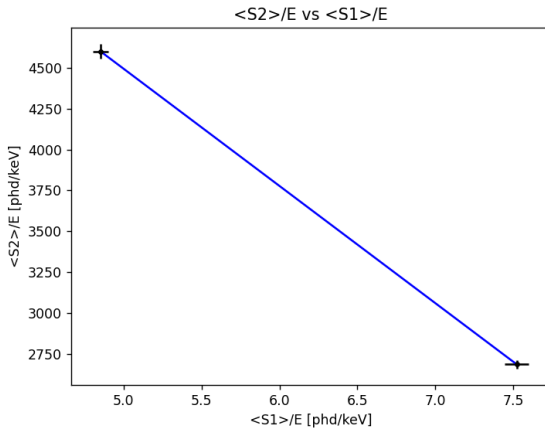


Figure 14. $\langle S2 \rangle / E$ vs $\langle S1 \rangle / E$ and fit used to obtain the values of the efficiency factors.

Using the parameters from the linear regression it was determined $g_1 = 0.154$ phd/ph and $g_2 = 110$ phd/e⁻.

With these two factors, it's possible to reconstruct the deposited energy from an interaction in the TPC.

3.4 Electronic Recoil Band

To discriminate electronic recoils from nuclear ones, the electronic recoil band Sec 2.3 was determined using data from simulations with Radon-220.

The Thorium-232 Decay Chain

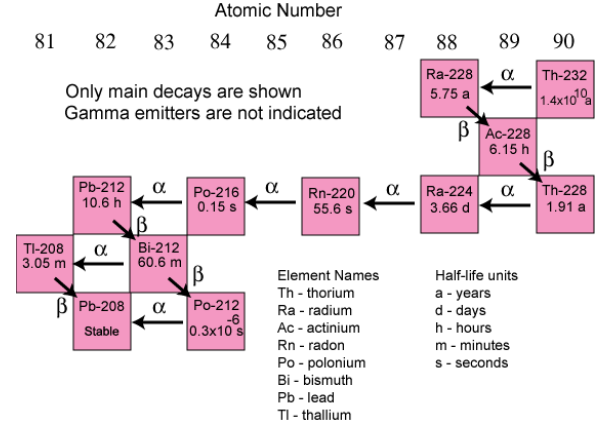


Figure 15. Thorium-232 chain decay.[16]

The Radon-220 belongs to the chain decay of Thorium-232, see Fig.15, and there are some beta decays after the appearance of Thorium-232. So the data obtained from simulations of Radon-220 in the TPC are appropriate to determine the Electronic Recoil Band. Primarily, it is necessary to obtain the medians of both S1 and $\log(S2)$, through binning the S1 data. Then, the electronic recoil band is considered as the zone limited by the fits of the S1 medians in function of the $\log(S2)$ medians $\pm 0.64 \times \sigma$, where σ is the standard deviation of the $\log(S2)$ of each bin, see Fig.16. Inside the electronic recoil band, there are 80% of events.

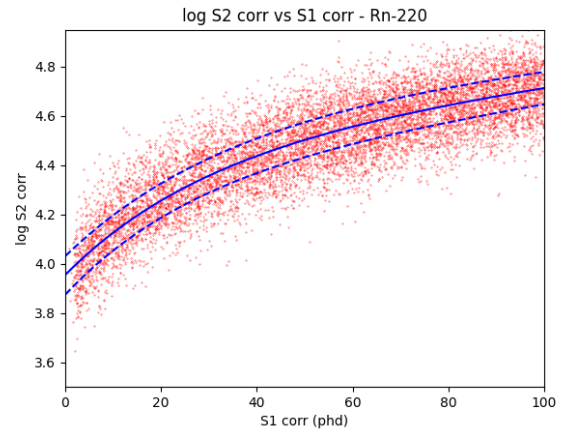


Figure 16. Electronic Recoil Band, the continuous curve was fitted with the median and the dashed curves are the $\pm 0.64 \times \sigma$ curves.

4 WIMP search

The curve that represent the median nuclear recoil band is given by:

$$\log(S2_{corr}) = a + b \cdot S1_{corr} - c \cdot \exp(-d \cdot S1_{corr}) \quad (4)$$

where $a = 4.2926$, $b = 1.3033 \times 10^{-3}$, $c = 5.6825 \times 10^{-1}$ and $d = 2.9654 \times 10^{-2}$

When applying the nuclear recoil median curve to the electronic events that occurred in the simulation of Radon-220 in the TPC, see Fig.17, only a few of these events appeared below the curve of the nuclear recoil band. This fraction of events below that curve is called the leakage fraction. The value obtained for the leakage fraction was 0.5%, so the electronic recoil rejection is 99.5% below the NR mean. This very good result verifies that it's possible to use the recoil bands to discriminate if a set of events is indeed nuclear recoils or electronic recoils.

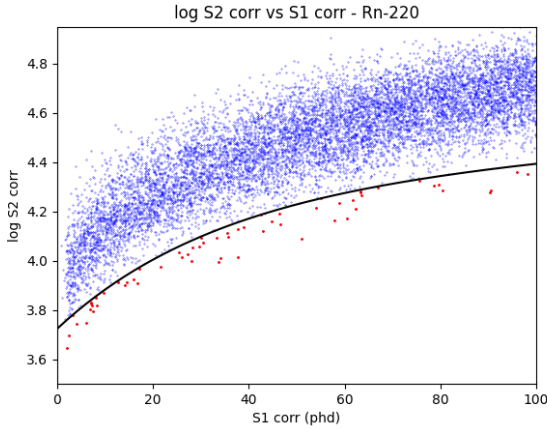


Figure 17. Electronic recoil rejection and the nuclear recoil median curve.

When applying the curve to the WIMP search data, see Fig.18, none of these events appear below the nuclear recoil band. So, according to this data, there's no evidence of WIMPs. With the leakage fraction value and the wimp search data, using the TROlke tool from the data analysis framework root[17], the value of the event limit above the background obtained was 3.4 events.

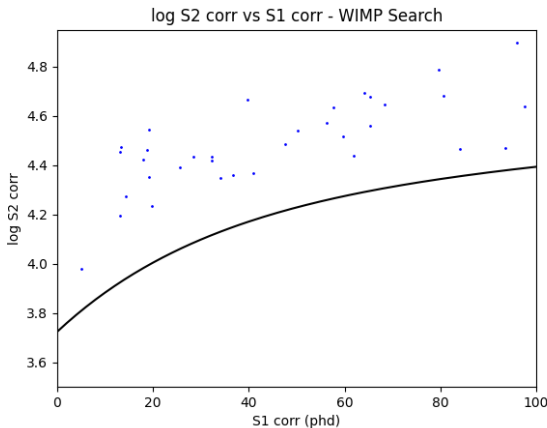


Figure 18. Wimp search simulated data.

4.1 Sensitivity

The expression 5 can be used to determine the dependence of the WIMP-nucleus cross-section with the mass of the WIMPs [18].

$$\widehat{R}_0 = \frac{2}{\sqrt{\pi}} \frac{N_A}{A} m_{FV} \frac{\rho_{DM}}{M_{DM}} \sigma_{WN} v_0 t_{exp} \epsilon_0 \quad (5)$$

Where \widehat{R}_0 is the event limit above the background, $N_A = 6.022 \times 10^{23} \text{ mol}^{-1}$ the Avogadro constant, $A = 131.293 \text{ g mol}^{-1}$ the molar mass of the Xenon target, m_{FV} the mass of fiducial volume, $\rho_{DM} = 0.4 \text{ GeV cm}^{-3}$ the local dark matter density, M_{DM} the mass of the WIMPs, $M_A = 122.026 \text{ GeV}/c^2$ the average mass of a Xe nucleus, $M_n = 0.939 \text{ GeV}/c^2$ the average mass of a Xe nucleon, σ_{WN} the WIMP-nucleus cross-section, σ_{Wn} the Spin Independent (SI) WIMP-nucleon cross-section, $v_0 = 2.2 \times 10^7 \text{ cm s}^{-1}$ the average galactic orbital velocity of the solar system, $t_{exp} = 1.296 \times 10^6 \text{ s}$ the exposure of the data, $E_0 = \frac{1}{2} M_{DM} v_0^2$ the incident kinetic energy of the WIMP, $E_{th} = 5.3 \text{ keV}$ the energy threshold of the LZ detector, E_R the energy of the recoiling nucleus from a WIMP elastic scatter, $r = \frac{4M_{DM}M_A}{(M_{DM}+M_A)^2}$ the kinetic factor, $\mu_{WN} = \frac{M_{DM}M_A}{M_{DM}+M_A}$ the reduced mass of WIMP-nucleus, $\mu_{Wn} = \frac{M_{DM}M_n}{M_{DM}+M_n}$ the reduced mass of WIMP-nucleon. The parameter ϵ_0 that appears in expression 5 is an experimental factor and can be computed using expression 6.

$$\epsilon_0 = \frac{1}{E_0 r} \int_{E_{th}}^{\infty} e^{-\frac{E_R}{E_0 r}} dE_R = e^{-\frac{E_{th}}{E_0 r}} \quad (6)$$

It was assumed that the fiducial volume is a cylinder with radius equal to 68 cm and height equal to 140 cm. Since the Xe density is equal to 2.9 g cm^{-3} the value of the mass of fiducial volume, m_{FV} , that is needed to compute the equation 5, is equal to $5.90 \times 10^6 \text{ g}$.

After the computation of the expression 5, the WIMP-nucleus cross-section in function of the mass of the WIMPs was obtained. This function can be used to determine the SI WIMP-nucleon cross-section in function of the mass of the WIMPs.

The expression 7 and 8 were used to obtain the value of WIMP-nucleus cross-section and the value of the SI WIMP-nucleon cross-section respectively (REF).

$$\sigma_{WN} = \frac{4}{\pi} \mu_{WN}^2 f_n^2 A^2 \quad (7)$$

$$\sigma_{Wn} = \frac{4}{\pi} \mu_{Wn}^2 f_n^2 \quad (8)$$

From the expressions 7 and 8, the expression 9 was obtained.

$$\sigma_{Wn} = \frac{\sigma_{WN} \mu_{Wn}^2}{A^2 \mu_{WN}^2} \quad (9)$$

With expression 9, it's possible to draw the SI WIMP-nucleon cross-section in function of the mass of the WIMPs. The Fig.19 shows that relationship.

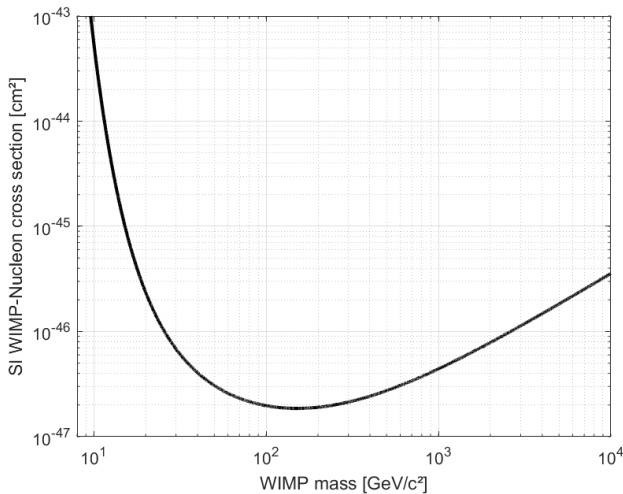


Figure 19. Sensitivity of LUX-ZEPLIN.

From the graph of the Fig.19 it can be concluded that the SI WIMP-nucleon cross-section for a WIMP mass of 150 GeV/c² is equal to $1.856 \times 10^{-47} \text{ cm}^2$. Fig.3.

5 Conclusion

This study used simulated LZ data, which has been calibrated with some conditions, and it showed that it is possible to discriminate nuclear recoils from electronic recoils to search for WIMPs. It was determined the variables $g_1 = 0.154 \text{ phd/ph}$ and $g_2 = 110 \text{ phd/e}^-$ allowing the determination of the energy deposited by interactions. The 15 days of data from the WIMP search showed no evidence of WIMPs. It was determined the sensitivity of LZ for the spin-independent WIMP-Nucleon cross-section of $1.856 \cdot 10^{-47} \text{ cm}^2$ for a WIMP mass of 150 GeV which is within the expected values for this exposition (5600 kg·15 days).

Acknowledgements

This paper presents the work done during our summer internship at LIP at the Universidade de Coimbra. We would like to thank LIP for the opportunity to take on this internship and learn more about this fascinating topic. We would also like to give a special thank to our coordinators, Cláudio Silva and Paulo Brás for all the help they provided during this internship.

References

- [1] A. Araujo, D.F. López, J.G. Pereira, *Gravitation and Cosmology* **25**, 157 (2019)
- [2] N. Aghanim, Y. Akrami, M. Ashdown, J. Aumont, C. Baccigalupi, M. Ballardini, A.J. Banday, R.B. Barreiro, N. Bartolo, S. Basak et al., *Astronomy & Astrophysics* **641**, A6 (2020)
- [3] R. Catena, P. Ullio, *Journal of Cosmology and Astroparticle Physics* **2010**, 004 (2010)
- [4] P.D. Group, P.A. Zyla, R.M. Barnett, J. Beringer, O. Dahl, D.A. Dwyer, D.E. Groom, C.J. Lin, K.S. Lugovsky, E. Pianori et al., *Progress of Theoretical and Experimental Physics* **2020** (2020)
- [5] D. Akerib, C. Akerlof, S. Alsum, H. Araújo, M. Arthurs, X. Bai, A. Bailey, J. Balajthy, S. Balashov, D. Bauer et al., *Physical Review D* **101** (2020)
- [6] J. Aalbers, D.S. Akerib, C.W. Akerlof, A.K.A. Musalhi, F. Alder, A. Alqahtani, S.K. Alsum, C.S. Amarasinghe, A. Ames, T.J. Anderson et al. (2022)
- [7] D. Akerib, C. Akerlof, D. Akimov, A. Alqahtani, S. Alsum, T. Anderson, N. Angelides, H. Araújo, A. Arbuckle, J. Armstrong et al., *Nuclear Instruments and Methods in Physics Research Section A: Accelerators, Spectrometers, Detectors and Associated Equipment* **953**, 163047 (2020)
- [8] D. Akerib, C. Akerlof, D. Akimov, A. Alqahtani, S. Alsum, T. Anderson, N. Angelides, H. Araújo, A. Arbuckle, J. Armstrong et al., *Nuclear Instruments and Methods in Physics Research Section A: Accelerators, Spectrometers, Detectors and Associated Equipment* **953**, 163047 (2020)
- [9] The LZ Collaboration, D.S. Akerib, C.W. Akerlof, D.Y. Akimov, S.K. Alsum, H.M. Araújo, X. Bai, A.J. Bailey, J. Balajthy, S. Balashov et al. (2015)
- [10] D. Akerib, S. Alsum, H. Araújo, X. Bai, A. Bailey, J. Balajthy, P. Beltrame, E. Bernard, A. Bernstein, T. Biesiadzinski et al., *Physical Review D* **97** (2018)
- [11] D. Akerib, C. Akerlof, A. Alqahtani, S. Alsum, T. Anderson, N. Angelides, H. Araújo, J. Armstrong, M. Arthurs, X. Bai et al., *Astroparticle Physics* **125**, 102480 (2021)
- [12] D. Akerib, C. Akerlof, S. Alsum, H. Araújo, M. Arthurs, X. Bai, A. Bailey, J. Balajthy, S. Balashov, D. Bauer et al., *Physical Review D* **101** (2018)
- [13] M. Szydagis, G.A. Block, C. Farquhar, A.J. Flesher, E.S. Kozlova, C. Levy, E.A. Mangus, M. Mooney, J. Mueller, G.R.C. Rischbieter et al., *Instruments* **5**, 13 (2021)
- [14] Y. Khazov, I. Mitropolsky, A. Rodionov, *Nuclear Data Sheets* **107**, 2715 (2006)
- [15] E. Browne, *Nuclear Data Sheets* **66**, 281 (1992)
- [16] T.M. Missimer, C. Teaf, R.G. Maliva, A. Danley-Thomson, D. Covert, M. Hegy, *International Journal of Environmental Research and Public Health* **16** (2019)
- [17] J. Conrad, J. Lundberg (2009), <https://root.cern/doc/v626/classTRolke.html>
- [18] J. Lewin, P. Smith, *Astroparticle Physics* **6**, 87 (1996)